PSFC/JA-14-40

Poloidal Asymmetries in Edge Transport Barriers

R. M. Churchill,[1, 2] C. Theiler,[1, 3] B. Lipschultz,[1, 4] I. H. Hutchinson,[1]
M. L. Reinke,[1, 4] D. Whyte,[1] J. W. Hughes,[1] P. Catto,[1] M. Landreman,[1, 5]
D. Ernst,[1] C. S. Chang,[2] R. Hager,[2] A. Hubbard,[1] P. Ennever,[1]
J. R. Walk,[1] and the Alcator C-Mod team

[1]Plasma Science and Fusion Center, Massachusetts Institute of Technology, Cambridge, Massachusetts 02139, USA
[2]Princeton Plasma Physics Laboratory, Princeton, New Jersey 08543, USA
[3]Centre de Recherches en Physique des Plasmas École Polytechnique Fédérale de Lausanne, CH-1015 Lausanne, Switzerland
[4]Department of Physics, University of York, Heslington, York YO10 5DD, UK
[5]Department of Physics, University of Maryland, College Park, Maryland 20742, USA

Plasma Science and Fusion Center
Massachusetts Institute of Technology
Cambridge MA 02139

This work was supported by the U.S. Department of Energy, Grant No. DE-FG02-91ER-54109. Reproduction, translation, publication, use and disposal, in whole or in part, by or for the United States government is permitted.

Accepted in the Physics of Plasmas (November 2014)

Poloidal asymmetries in edge transport barriers

R. M. Churchill,[1, 2, a)] C. Theiler,[1, 3] B. Lipschultz,[1, 4] I. H. Hutchinson,[1] M. L. Reinke,[1, 4] D. Whyte,[1] J. W. Hughes,[1] P. Catto,[1] M. Landreman,[1, 5] D. Ernst,[1] C. S. Chang,[2] R. Hager,[2] A. Hubbard,[1] P. Ennever,[1] J. R. Walk,[1] and the Alcator C-Mod team

[1)] *Plasma Science and Fusion Center, Massachusetts Institute of Technology, Cambridge, Massachusetts 02139, USA*

[2)] *Princeton Plasma Physics Laboratory, Princeton, New Jersey 08543, USA*

[3)] *Centre de Recherches en Physique des Plasmas École Polytechnique Fédérale de Lausanne, CH-1015 Lausanne, Switzerland*

[4)] *Department of Physics, University of York, Heslington, York YO10 5DD, UK*

[5)] *Department of Physics, University of Maryland, College Park, Maryland 20742, USA*

Measurements of impurities in Alcator C-Mod indicate that in the pedestal region significant poloidal asymmetries can exist in the impurity density, ion temperature, and main ion density. In light of the observation that ion temperature and electrostatic potential are not constant on a flux surface [Theiler, *Nucl. Fus.*, 2014], a technique based on total pressure conservation to align profiles measured at separate poloidal locations is presented and applied. Gyrokinetic neoclassical simulations with XGCa support the observed large poloidal variations in ion temperature and density, and that the total pressure is approximately constant on a flux surface. With the updated alignment technique, the observed in-out asymmetry in impurity density is reduced from previous publishings [Churchill, *Nucl. Fus.*, 2013], but remains substantial ($n_{z,H}/n_{z,L} \sim 6$). Candidate asymmetry drivers are explored, showing that neither non-uniform impurity sources nor localized fluctuation-driven transport are able to explain satisfactorily the impurity density asymmetry. Since impurity density asymmetries are only present in plasmas with strong electron density gradients, and radial transport timescales become comparable to parallel transport timescales in the pedestal region, it is suggested that global transport effects relating to the strong electron density gradients in the pedestal are the main driver for the pedestal in-out impurity density asymmetry.

PACS numbers: 52.25.Vy

[a)]Electronic mail: rchurchi@pppl.gov

I. INTRODUCTION

In a previously published letter[1], we presented initial results of a measured in-out impurity density asymmetry in the pedestal region of Alcator C-Mod. In this paper, additional data and analysis are presented, focusing on possible mechanisms which can drive such an impurity asymmetry. Understanding the origin of these asymmetries will aid in forming a complete picture of the global transport of impurities throughout the plasma, and the structure and nature of edge transport barriers.

The results from the previous letter[1] showed that an in-out B^{5+} impurity density asymmetry is formed in the pedestal region, with impurity densities greater on the high-field side. The magnitude of the asymmetry was large, reaching levels of $n_{z,H}/n_{z,L} \gtrsim 10$, where H and L refer to the high-field side (HFS) and low-field side (LFS) respectively. This magnitude is larger than allowed by standard neoclassical transport[2–5] (in this paper, standard neoclassical transport will refer to transport derived assuming the main ion poloidal Larmor radius is much smaller than the perpendicular gradient scale lengths in ion density or temperature, $\rho_{\theta,i} \ll L_\perp$). The impurity density asymmetry was present in plasmas with strong electron density gradients, namely H-mode plasmas. In plasmas without an electron density pedestal, even those with strong temperature pedestals such as I-mode[6], the measured impurity density at the LFS and HFS matched, suggesting the electron density pedestal is a necessary condition to drive the in-out impurity density asymmetry. We also observed that in H-mode the LFS impurity density pedestal location shifts inward and the width increases as plasma current decreases. In contrast, the HFS impurity density pedestal location and width remained approximately fixed with changing plasma current.

Because of uncertainties in the reconstruction of flux surface position, there is uncertainty at the level of a few millimeters, in the registration ("alignment") of the flux surfaces with the absolute positions at the inboard and outboard sides. In previous work[1], we made the ansatz that the impurity temperature T_z is uniform on a flux surface, and we shifted the apparent positions accordingly. However, the constancy of T_z on a flux surface was called into question by measurements of T_z and E_r at the LFS and HFS[7]. We here assume instead that total pressure is constant on a flux surface, and we derive the consequences for the interpretation of the measurements[1,8], including electron density asymmetries in the pedestal region.

Several mechanisms could be responsible for these asymmetries, among them fluctuations, strong local sources, and collisional transport. As mentioned, the main focus of this paper is to explore these drives, and determine which can be primarily responsible for the asymmetries observed in the pedestal region of Alcator C-Mod.

The outline of this paper is as follows. In Section II, we introduce the updated alignment technique. Section III explores electron density asymmetries in light of the updated profile alignment. Section IV presents XGCa simulation results confirming the poloidal variation of main ion density and temperature. Section V presents further experimental results of the impurity density and temperature asymmetry. In Section VI impurity transport modelling of boron in the pedestal is described using the impurity transport modelling code STRAHL. Section VII explores various candidates which may cause the impurity density asymmetry in the pedestal.

II. PROFILE ALIGNMENT

The comparison of measured profiles at different poloidal locations, such as the LFS and HFS midplanes, requires accurate spatial calibrations and magnetic reconstructions. For profiles with strong gradients, small displacements give rise to large changes in the apparent values. To overcome systematic and random errors in the EFIT magnetic reconstruction, the location of the flux surfaces in the vicinity of the measured profiles is usually adjusted, based on the measured profiles themselves and physical assumptions. In general, we wish to align three sets of quantities relative to each other:

1. Impurity profiles of density, temperature and velocity (n_{zL}, T_{zL}, V_{zL}), measured at the LFS midplane with the LFS GP-CXRS system[9]
2. Impurity profiles (n_{zH}, T_{zH}, V_{zH}) measured at the HFS midplane with HFS GP-CXRS
3. Electron density and temperature profiles (n_e, T_e) measured at the top of the plasma with Thomson Scattering[10].

It's also desirable to align the profiles to their absolute location with respect to the separatrix, however this does not affect the flux-surface asymmetry results.

A. Previous Alignment Based on Temperature Equilibration

In past studies[1,11,12] using the CXRS system on Alcator C-Mod, impurity profiles were aligned so that both the LFS and HFS impurity temperature profiles matched the electron temperature profile. This will be referred to as the T_z-alignment. This alignment was based on two arguments: (1) the electrons and ions are thermally well coupled due to the high collisionality of most C-Mod plasmas, and (2) the poloidal variation of the electron temperature is low since the parallel heat conduction to the divertor sets a stringent requirement on the electron temperature at the separatrix[13,14] (usually $T_e \sim 100$ eV in H-mode plasmas).

However, using T_z-alignment, a significant shift between the LFS and HFS E_r profiles was obtained[7] (see the middle column of Figure 1 for an example). This in turn would lead to a large poloidal variation in the electrostatic potential ($\Phi = \Phi_0 - \int_{r_0}^{r} dr E_r$, where Φ_0 is the electrostatic potential at position r_0, and r is a real space coordinate). Normally, both temperature and electrostatic potential (Φ) are considered to be flux functions to lowest order[15,16]. Therefore the assumptions of the T_z-alignment must be re-evaluated.

B. Profile Alignment Satisfying Parallel Momentum Conservation

In order to determine a more satisfactory alignment of the LFS and HFS profiles, a solution was sought which satisfied parallel momentum balance. We will use the general momentum conservation equation for any species j ignoring external momentum sources:

$$m_j n_j \left(\frac{\partial \mathbf{V}_j}{\partial t} + \mathbf{V}_j \cdot \nabla \mathbf{V}_j \right) = -\nabla p_j - \nabla \cdot \overleftrightarrow{\pi}_j + Z_j e n_j \left(\mathbf{E} + \mathbf{V}_j \times \mathbf{B} \right) + \mathbf{R}_j \tag{1}$$

where all terms have their usual meaning, with π_j the pressure anisotropy and R_j the friction force between species j and all other plasma species.

1. Electron Profile Alignment

For the electrons we can neglect the electron inertia, viscosity, and friction[8]. If we assume the electron temperature is constant on a flux surface[7], we can solve the electron parallel momentum equation directly, which results in a Boltzmann relation for the electrons:

$$n_e(\psi,\theta) = n_{eL} \exp\left(\frac{e}{T_e}\left[\Phi(\psi,\theta) - \Phi_L\right]\right) \tag{2}$$

where subscript 'L' refers to quantities at the LFS. This equation shows that the poloidal variation of the electron density is directly related to the poloidal variation of the electric potential.

The assumption that T_e is constant on a flux surface[7,17–19] is based on the fact that electron parallel heat conductivity is rapid: greater than ion parallel conductivity by a factor of approximately $\sqrt{m_D/m_e} \sim 60$. The electron profiles are aligned such that the electron temperature at the separatrix satisfies constraints set by parallel heat conduction to the divertor[13,14].

2. Impurity Profiles - Relative Alignment

We now determine the alignment of the LFS/HFS impurity profiles *relative* to each other. Consider the total parallel momentum equation: the sum of the individual parallel momentum equations for electrons, main ions, and a single impurity ion species. The friction forces cancel, since by definition $\mathbf{R}_{jk} = -\mathbf{R}_{kj}$, and so $\sum_{j=e,i,Z} \mathbf{R}_j = 0$. The electric potential term will also disappear, as the prefix is $n_i + Zn_z - n_e$, which due to quasi-neutrality is identically 0. Assuming trace impurity levels[8], this reduces to:

$$\mathbf{b}\cdot\nabla(p_e + p_i) = -m_i n_i \mathbf{b}\cdot\mathbf{V_i}\cdot\nabla\mathbf{V_i} - \mathbf{b}\cdot\nabla\cdot\overleftrightarrow{\pi}_i \tag{3}$$

The main ion inertia and viscosity terms shown in Equation 3 may be significant in the pedestal region if the parallel ion flow approaches the sound speed. We assume (admittedly without complete justification) that those terms can be ignored. Then $\mathbf{b}\cdot\nabla(p_e + p_i) \approx 0$, i.e. the total plasma pressure is constant on a flux surface. The poloidal variation of n_e and Φ can then be solved for[7,8]:

$$\boxed{\begin{aligned} n_e(\psi,\theta) &= \frac{T_e + T_{zL}}{T_e + T_z} n_{eL} \\ \Phi(\psi,\theta) &= \Phi_L + \frac{T_e}{e}\ln\left(\frac{T_e + T_{zL}}{T_e + T_z}\right) \end{aligned}} \tag{4}$$

Note that we have assumed $T_i = T_z$, as the ion-impurity energy equilibration is much faster than the processes that drive poloidal temperature asymmetries, or the ion-electron energy equilibration time[7].

The expected E_r at the HFS can then be calculated from Equation 4 with the relation $E_r = -\frac{\partial \Phi}{\partial r}$, so at the high-field side (subscript H):

$$\begin{aligned} E_{rH} &= -\frac{\partial \Phi}{\partial r}\bigg|_H \\ &= \frac{dr_L}{dr_H} E_{rL} - \frac{\partial}{\partial r_H}\left[\frac{T_e}{e}\ln\left(\frac{T_e + T_{zL}}{T_e + T_{zH}}\right)\right]. \end{aligned} \tag{5}$$

The resulting equation for the HFS E_r depends only on quantities which we measure (except for dr_L/dr_H, i.e. the flux expansion at the LFS and HFS, which is taken from EFIT with negligible error). Using the measured profiles of T_e, T_{zL}, T_{zH}, and E_{rL}, we can optimize the shift between the LFS and HFS impurity profiles until the measured HFS E_r best matches the expected HFS E_r from Equation 5.

In all experimental cases studied, the second term on the RHS of Equation 5 makes a smaller contribution than the first term, the LFS E_r (because of the logarithmic sensitivity of the predicted radial electric field to in-out temperature asymmetries). This means that the measured E_{rL} and E_{rH} by themselves can be used to give an approximate *relative* alignment of the LFS and HFS impurity profiles. Equivalently, the edge impurity poloidal velocity could be used, since the calculated E_r well position for the LFS or HFS on C-Mod is mainly determined by the location of the peak in the impurity poloidal velocity[8,11].

3. Impurity Profiles - Absolute Alignment

While the *relative* alignment of the LFS and HFS impurity profiles is well constrained by Equation 5, due to the dominance of the E_r term, the absolute alignment of these profiles to the electron profiles has a wide range of possibilities within the error bars of the measurements. In order to align the impurity profiles relative to the electron profiles (i.e. to the separatrix) we will make the ansatz that the top of the impurity ion temperature pedestals are *at or outside* of the top of the electron temperature pedestal. This tends to locate the E_r well minimum measured from the impurity profiles at the LFS and HFS close to the minimum in the E_r diamagnetic term calculated from the electron n_e and T_e profiles. Although this leaves the impurity profiles under-constrained in their alignment

to the electron profiles, it has a negligible effect on the *relative* LFS to HFS impurity profile alignment, as the expected HFS E_r in Equation 5 is relatively insensitive to the poloidal variation of the ion temperature. Furthermore, the impurity density calculation is negligibly affected by small shifts of n_e and T_e around this nominal alignment. This alignment procedure, based on satisfying total pressure (electron and main ion) constancy on a flux surface, will be referred to as "total pressure"-alignment.

An example of the T_z- and total pressure-alignment procedure is shown in Figure 1. The first column shows the original, unshifted radial electric field, temperature, and density, mapped using normal EFIT. The horizontal coordinate used in the plot, ρ, is the normalized LFS midplane major radius[1], which is close to r/a, with r the distance from the magnetic axis and a the minor radius. The second column in Figure 1 shows the profiles aligned to match all temperatures, which shows the mismatch[7] of the measured LFS and HFS E_r[20]. The final column shows total pressure-alignment. In this alignment, both the LFS and HFS T_z pedestals are at or further out from the T_e pedestal, and the measured LFS and HFS E_r wells have only a slight shift, due to the second term on the right hand side of Equation 5. In total, the applied shifts for the LFS system are $\Delta\rho \sim 0.032$, or $\sim$7 mm, while for the HFS system they are $\Delta \sim 0.0061$, or $\sim$1.4 mm. It should be noted that within the error bars, there is an additional allowable shift of $\rho \sim 0.002$ which still satisfies matching the HFS E_r to the calculated HFS E_r.

To summarize the total-pressure alignment procedure used throughout this paper, the electron T_e profile is used to *absolutely* constrain the position of the measured electron profiles to its corresponding flux surfaces in the plasma (i.e. to the separatrix). T_e is assumed to be a flux function, while n_e is allowed to vary poloidally, determined by the poloidal variation in electric potential, Φ. The LFS and HFS impurity profiles are shifted such that the measured T_z pedestal top location is *at or outward* of the T_e pedestal top. The LFS and HFS impurity profiles are aligned *relative* to each other by matching the expected HFS E_r to the measured HFS E_r, using Equation 5.

III. ELECTRON DENSITY ASYMMETRIES

In either the T_z- or total pressure-alignment, an asymmetry between the LFS and HFS E_r results, leading to an electron density asymmetry through the Boltzmann relation, Equation

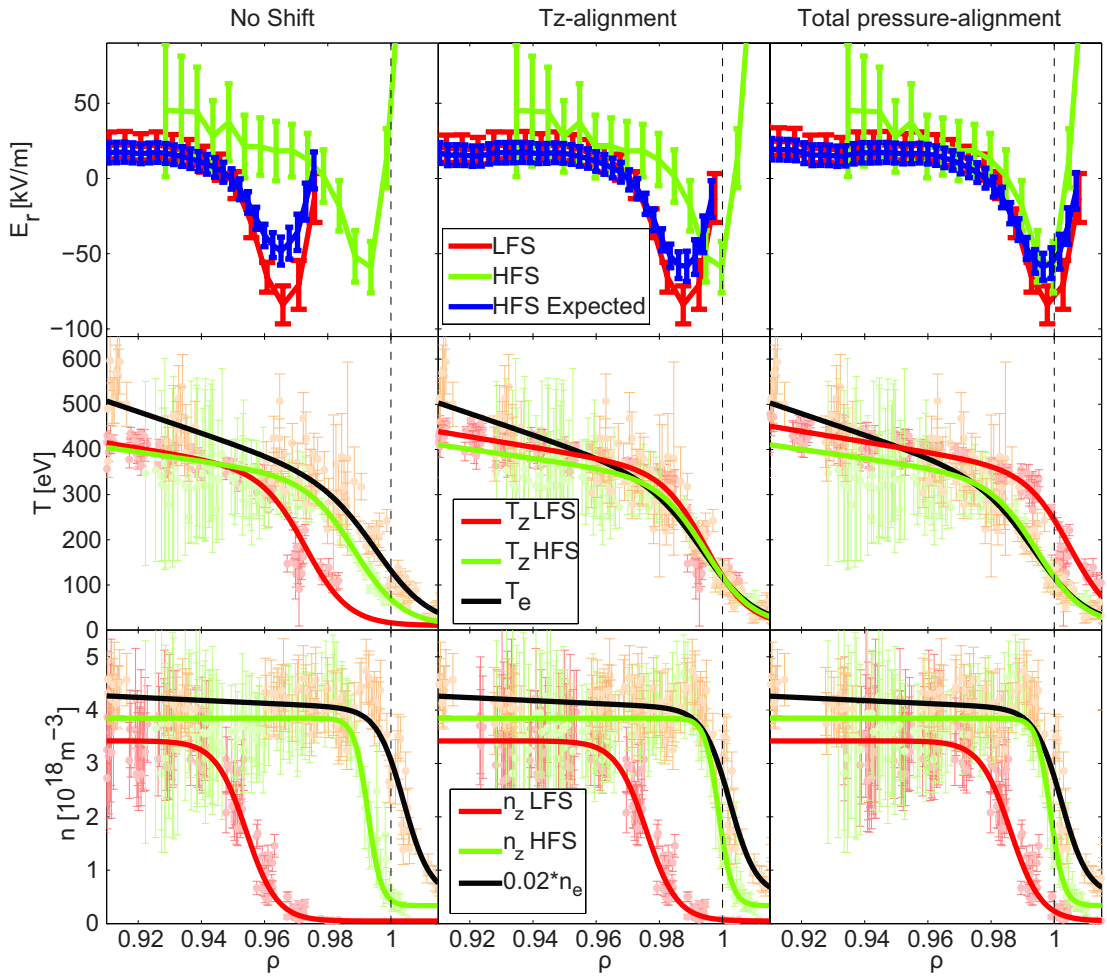

FIG. 1: Example of the alignment technique for profiles in an EDA H-mode. In the first column are shown profiles mapped using the EFIT magnetic reconstruction with their calibrated position. The second column shows the profiles when the LFS and HFS T_z profiles are matched. The third column shows the alignment procedure used throughout this paper, the total pressure-alignment, where profiles are shifted until the HFS measured E_r matches the expected (Equation 5).

2. For the T_z-alignment, the HFS n_e pedestal would be significantly shifted towards the core compared to the LFS n_e pedestal, based on the measured E_r in the middle column of Figure 1. For the total pressure-alignment, the HFS n_e pedestal based on the potential asymmetry would be shifted further outward than the LFS n_e profile, and the n_e asymmetry would be

much smaller in magnitude than in the T_z-alignment case.

An example of the expected HFS n_e in the total pressure-alignment is shown in Figure 2, derived using Equation 4 with the radial electric fields from the third column of Figure 1. Also shown in the lower plot of Figure 2 is the asymmetry factor, $A = n_{eH}/n_{eL}$, reaching a maximum value of $\sim$2.

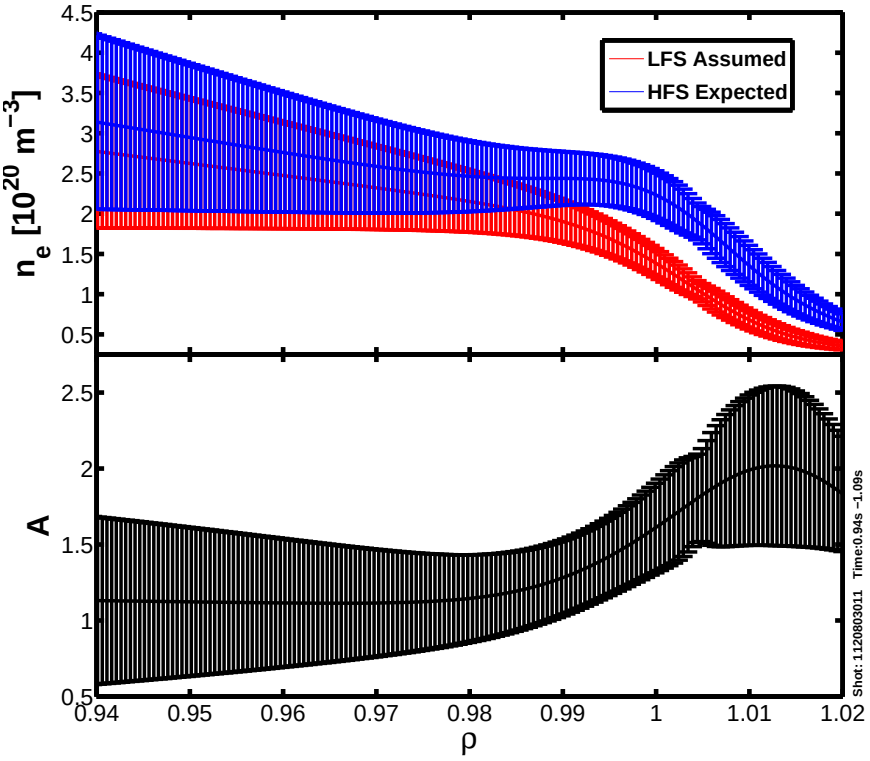

FIG. 2: Expected HFS electron density from Equation 4, based on the measured impurity temperature asymmetry and an assumed LFS electron density profile. This assumed LFS n_e profile is based on measurements of n_e at the top of the plasma. Because of the chosen absolute alignment of the impurities to the electrons, the asymmetry factor A_{n_e} is an upper limit. The lower limit A_{n_e} would have a peak of 1.5.

As this is a sizeable difference in electron density, it might be independently detectable by the measured D_α radiance from the LFS and HFS gas puff[9], $I_{D_\alpha} = \frac{1}{4\pi}\int d\ell\, PEC_{32}^{EXC} n_D n_e$ (PEC is the photon emissivity coefficient for the D_α transition, n_D the neutral density, and ℓ the viewing sightline). Qualitatively, the gas puff neutral density, and therefore D_α radiance, will decrease sharply in the region of the electron density pedestal. Unfortunately,

the instantaneous flow rate for each separate GP-CXRS LFS and HFS gas delivery capillary is not well characterized[9], making comparisons of the absolute values of I_{D_α} between the LFS and HFS unusable. However, the maximum in the absolute value of the inverse gradient scale lengths of D_α radiance, $\left|L^{-1}_{I_{D_\alpha}}\right|$, can indicate the location of the electron density pedestal. The measured inverse gradient scale lengths of D_α radiance for the LFS and HFS are shown in Figure 3. The vertical lines shown are the expected location of the maximum in $L^{-1}_{D_\alpha}$, obtained from OSM-EIRENE of the gas puff neutral density[9]. The solid vertical lines show a simulation when background parameters are flux functions, and the dashed vertical lines shows a simulation when T_z and n_e vary, as shown in Figure 1 and 2. As seen in Figure 3, the location of maximum measured LFS $L^{-1}_{D_\alpha}$ matches well with the simulation. The HFS is closer to the total pressure-aligned case, but sits in between the two cases, suggesting the electron density pedestal could be further outward at the HFS. Additionally, the magnitude of the inverse gradient scale length is much larger at the HFS, which can not be explained by flux-surface spacing, indicating that the HFS n_e profile may also be narrower in width in flux space.

A poloidally varying electron density will *not* have a large effect on the derived impurity density, which depends on n_e through the CX rate coefficient and the ADAS PEC coefficients[9]. The atomic physics prefactor in the impurity density equation[1,9] varies by less than 20% for the density and temperature ranges of the C-Mod pedestal, except at the low density ($<2 \times 10^{19}\mathrm{m}^{-3}$) and temperatures ($<$100 eV) range, which anyway won't affect the impurity density except slightly at the very bottom of the pedestal. The effect of electron density variation on the calculated impurity density is essentially encoded in the measured D_α radiance.

In conclusion, the measured D_α gradient scale lengths at the LFS and HFS give support to the possibility of a poloidally varying electron density. The results can't conclusively confirm whether there is a higher n_e on the HFS as would result from the total pressure-alignment, but they do rule out a HFS n_e pedestal which is much further inward, as would be suggested by the variation in electric potential when profiles are T_z-aligned.

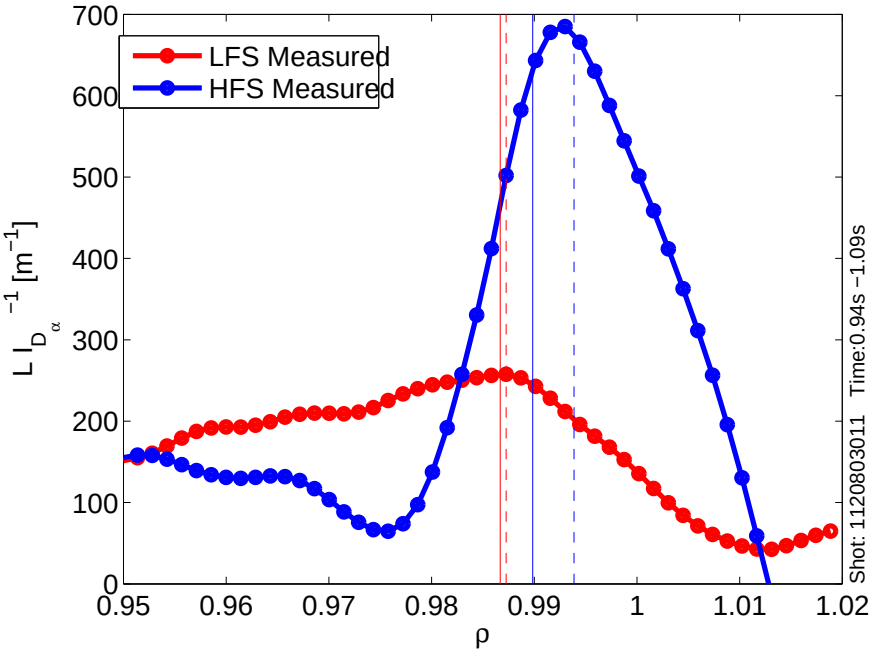

FIG. 3: Comparison of measured gradient scale lengths of I_{D_α} for the LFS and HFS. Vertical lines indicate the radial location of the maximum in $L_{I_{D\alpha}}$ from two separate OSM-EIRENE simulations: (1) Uniform, where n_e, T_e, and T_i are flux functions (solid) and (2) total pressure-aligned, where n_e and T_i vary poloidally (dashed).

IV. XGCA SIMULATIONS

To further understand the possible poloidal variation in ion temperature and electrostatic potential in the pedestal region, simulations of Alcator C-Mod were undertaken with the XGCa code, a total-f gyrokinetic neoclassical PIC code which is the axisymmetric version of XGC1[21]. To accurately simulate the pedestal region of Alcator C-Mod, a total-f code is needed since usually $\rho_{\theta,i} \sim L_{n_i}, L_{T_i}$. XGCa includes realistic magnetic geometry, including the separatrix. However, impurities are currently not included in XGCa, and so only the poloidal variation in main ion temperature, electron density, and electrostatic potential will be investigated here.

Inputs into this XGCa simulation were the measured electron density and the electron temperature as flux functions, with T_i initially set equal to T_e. The code then advances particles consistent with the total-f particle distribution equation and the axisymmetric gyrokinetic Poisson equation. This evolves the particle distributions, and hence n_e, T_e, T_i, and

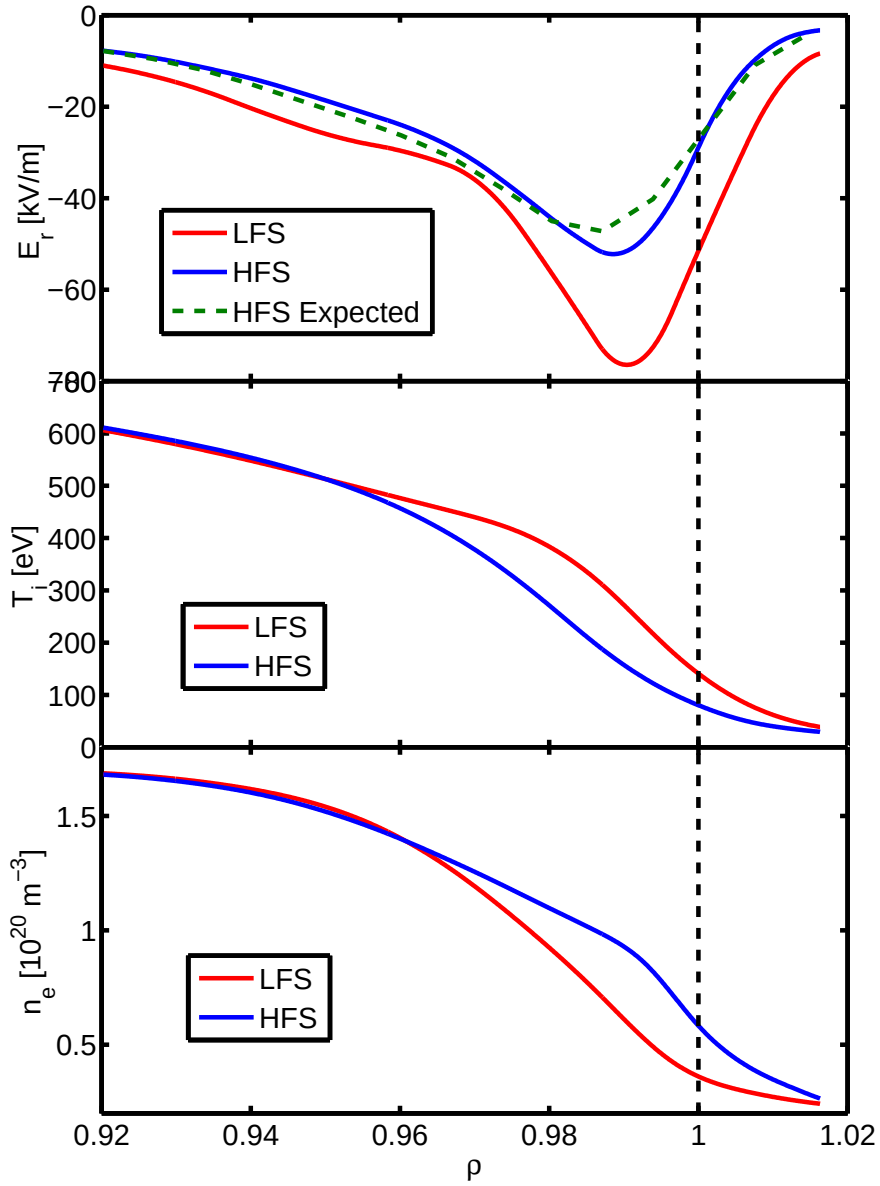

FIG. 4: XGCa simulation results of an EDA H-mode in Alcator C-Mod showing LFS and HFS results of (a) radial electric field, (b) main ion temperature, and (c) electron density. The HFS expected E_r is calculated from Equation 5. These results are in close agreement with observed experimental asymmetries. Note this simulation is of a different experimental discharge than the measurements in Figure 1.

Φ profiles. A realistic sheath boundary condition is set at the wall. Heating and particle

sources were not included in this simulation, as the total simulation time was limited to ∼4.5 ion toroidal transit times, corresponding to ∼2.5 ion collision times[15] at the pedestal top ($\rho \sim 0.975$), and ∼8.6 ion collision times at the pedestal foot ($\rho \sim 1.0$). Since no model for anomalous transport was used in these simulations, the plasma profiles evolve slowly compared to the collision time scale due to neoclassical transport alone. The poloidal structures of density, temperature and potential, however, form on the ion collision time scale. A couple of ion collision times into the simulation, they evolve slowly together with the plasma profiles. Therefore, even without sources or sinks, the simulation can be considered to be in a neoclassical "quasi-equilibrium" in this situation (addition of the neutral particle source and plasma turbulence could be considered in a future simulation for a more self-consistent study). This interpretation was confirmed by running the Eulerian neoclassical code NEO[22] using the profiles of density, temperature and electrostatic potential of a randomly selected time slice of the XGCa simulation (in quasi-steady state). Where NEO's approximations ($\rho_{\theta,i} \ll L_n, L_{T_i}$) are valid, good agreement was observed.

Results for an XGCa simulation of an EDA H-mode on C-Mod are shown in Figure 4. Three main results are seen from Figure 4: (1) the radial electric field is closely aligned between the LFS and HFS, with an asymmetry in the electric potential reaching a maximum of $e(\Phi_H - \Phi_L)/T_e \sim 0.6$, (2) the main ion temperature does exhibit a significant out-in asymmetry, here reaching $T_{i,L}/T_{i,H} \sim 1.8$; the difference being 125 eV, (3) the electron density exhibits an in-out asymmetry, with $n_{e,H}/n_{e,L} \sim 1.7$. These three simulation results match very well with the conclusions drawn from the C-Mod experimental results using the total pressure-alignment. Indeed, the total pressure $p_e + p_i$ from the XGCa simulation is very symmetric between the LFS and HFS, with a maximum variation of 18%. The assertion that the total pressure is approximately constant on a flux surface is thus well founded based on these XGCa simulation results.

The poloidal variation of the parallel ion flow obtained (not shown) is qualitatively similar to the variation obtained with the PERFECT code[23], for a steep pedestal density gradient. In that work the poloidal variation is due in part to the strong radial variation of the parallel flow, which produces a finite divergence in the pedestal which is negligible in the core. Further investigations will seek to identify if similar mechanisms cause the poloidal variation observed in the XGCa simulations.

These XGCa simulation results give confidence in the total pressure-alignment, including

the findings of significant asymmetries in ion temperature and electron density. Unless explicitly stated otherwise, the following experimental profiles will be aligned exclusively using the total pressure-alignment.

V. IN-OUT ASYMMETRIES IN THE PEDESTAL REGION

Impurity density asymmetries are observed in all flavors of H-mode in Alcator C-Mod[1,8]. When aligning LFS/HFS impurity profiles using the total pressure-alignment technique, the impurity density asymmetry is considerably reduced from that which resulted from aligning by T_z, but still very large. Figure 5 shows the impurity density asymmetry ratio, $A_{n_z} = n_{zH}/n_{zL}$, that results when using the two different alignments, T_z-alignment and total pressure-alignment, for a number of EDA H-modes.

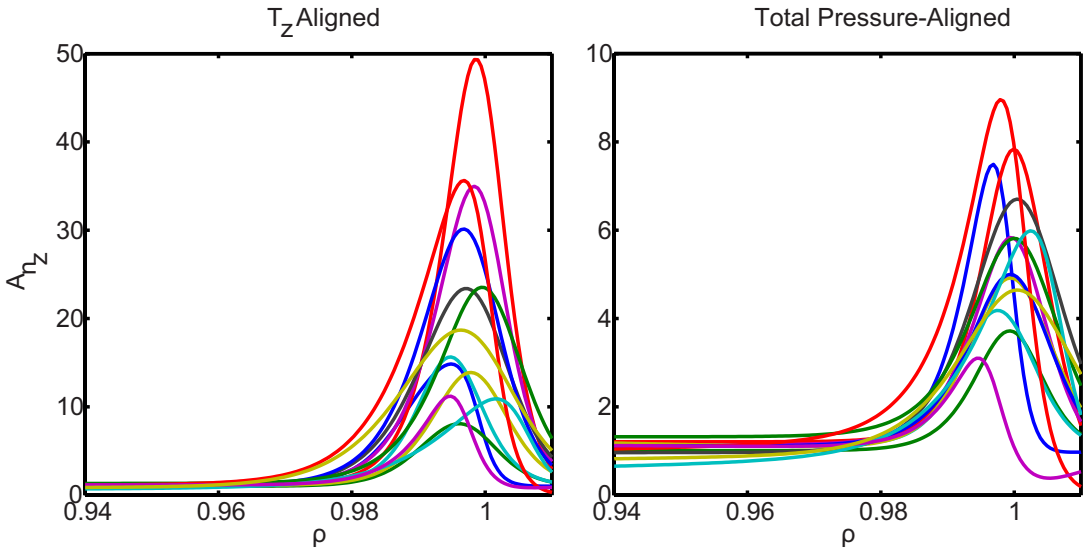

FIG. 5: Example density asymmetry ratios A_{n_z} for several EDA H-modes: (a) T_z-aligned profiles and (b) total pressure-aligned profiles. Note the different y-scales, showing that there is a large reduction in asymmetry ratios when using the total pressure-alignment.

A very interesting result going from the T_z-alignment to the total pressure-alignment (see Section II) is that the impurity pressure asymmetry is also reduced, even more than the density asymmetry since an out-in temperature asymmetry also results. This can be seen from the relative profile shifts in Figure 1 for the different alignments. We show in Figure 6 asymmetry factors, e.g. $n_z^{cos} = (A_{n_z} - 1)/(A_{n_z} + 1)$, for impurity density, temperature, and

pressure (n_z^{cos}, T_z^{cos}, and p_z^{cos}) in the two different alignments.

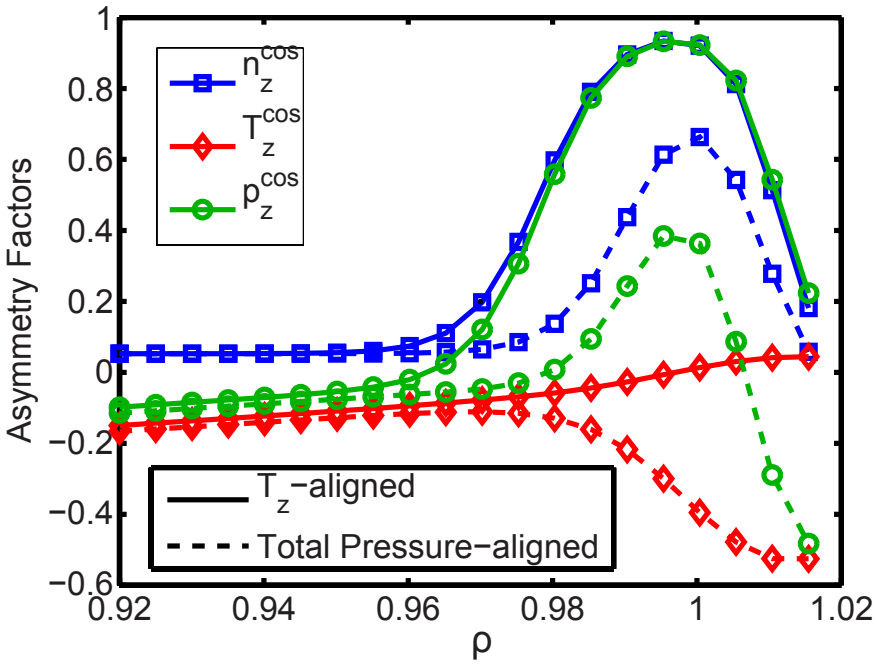

FIG. 6: Asymmetry factors for impurity density (n_z^{cos}), temperature (T_z^{cos}), and pressure (p_z^{cos}), using both the T_z-alignment and total pressure-alignment. The total pressure-alignment has a reduced impurity pressure asymmetry, due to the reduction of the density asymmetry, and formation of an opposing temperature asymmetry.

Plotted in Figure 7 is the difference between the B^{5+} density pedestal location at the HFS and the LFS, $\Delta\rho_{ped} = \rho_{ped,HFS} - \rho_{ped,LFS}$ as a function of the edge safety factor, q_{95}, for several H-mode discharges. $\Delta\rho_{ped}$ is shown for when profiles are T_z-aligned (in blue) and total pressure-aligned (red). An upward trend in $\Delta\rho_{ped}$ with q_{95} is seen. The trend remains relatively unchanged for the different alignments, though in the total pressure-alignment $\Delta\rho_{ped}$ increases slightly slower with q_{95} (here B_ζ was basically fixed, so this corresponds to lower I_p).

Also shown in Figure 7 are results from a previous study on C-Mod[24], which measured the hydrogen-like fluorine emission at the top of the plasma and at the LFS midplane using a line-integrated measurement of the soft X-ray emission[25]. The spacing between the pedestal locations is similar for the two impurity species, though for fluorine increases more strongly with q_{95}. This may indicate a significant up-down component in the poloidal variation of the impurity density, however without additional information on the B^{5+} at the top of the

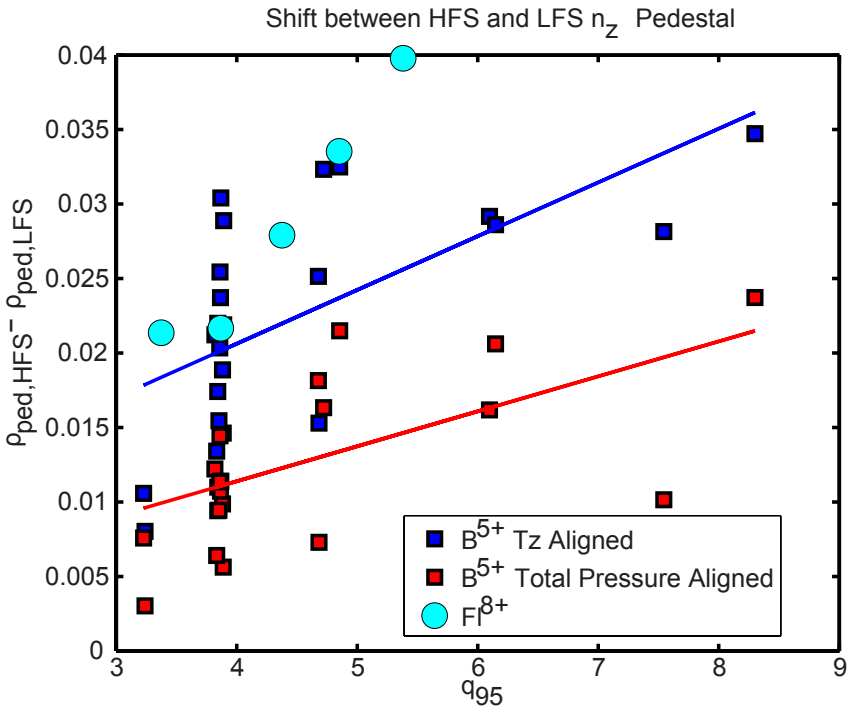

FIG. 7: Difference between the HFS and LFS n_z pedestal locations ($\rho_{ped,HFS} - \rho_{ped,LFS}$) versus the edge safety factor (q_{95}). Blue results are when using the T_z-alignment, red results are when using the total pressure-alignment. Data in light blue is taken from previous results for fluorine[24], measured at the top and LFS midplane.

plasma, or Fl^{8+} at the HFS midplane, this remains speculative.

The growing difference in H-mode plasmas between the $n_{B^{5+}}$ pedestal location for the LFS and HFS isn't just a simple shift, but rather the pedestal width on the LFS is also increasing with q_{95}, similar to electron density pedestal behavior[26]. For all the different regimes, the HFS boron density pedestal remains relatively fixed in width and position, while the LFS boron density pedestal width increases and the pedestal position shifts slightly inward depending on plasma parameters, as shown for the H-mode cases in Figure 8. This is suggestive that transport is changing locally at the LFS, possibly due to ballooning (i.e. stronger at the LFS) processes, such as collisional transport or certain turbulent modes.

Regardless of uncertainties in LFS/HFS profile alignment, the relative locations of the impurity density and temperature pedestal are different on the LFS and HFS in H-mode. On the LFS, the temperature pedestal is much further out than the impurity density pedestal. The HFS on the other hand has almost matching n_z and T_z pedestal locations, with the

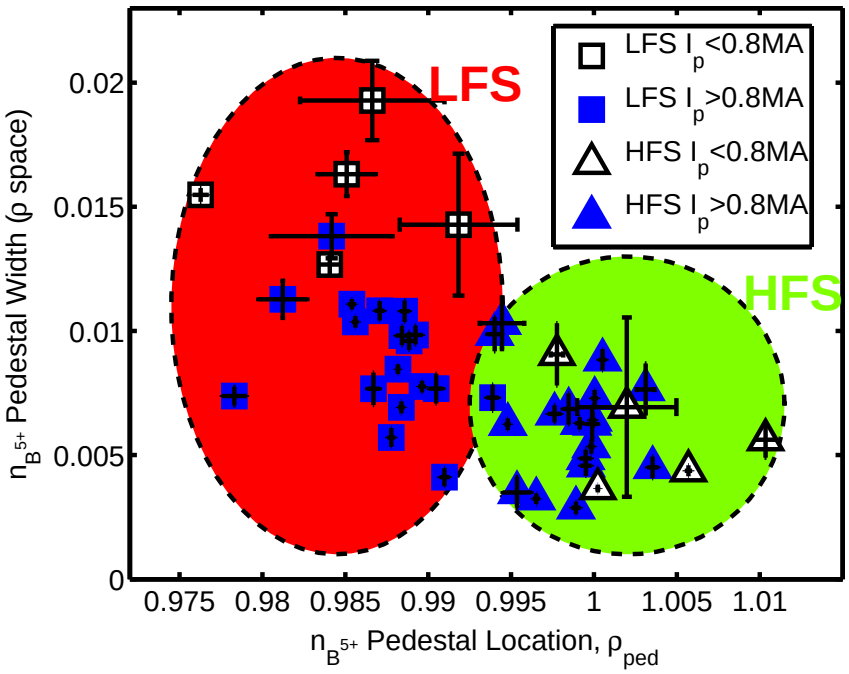

FIG. 8: Impurity density pedestal location (ρ_{ped}) vs width for the LFS and HFS. For lower I_p plasmas, the LFS pedestal width increases significantly.

density pedestal shifting slightly inward for lower plasma current discharges. These statements are shown graphically in Figure 9. Note that the electron density and temperature pedestals tend to align[26], similar to the HFS impurity density and temperature profiles.

VI. SIMULATED IMPURITY RADIAL DENSITY PROFILE

A natural question to ask is: what is the expected impurity density profile based on collisional transport and atomic physics? There is evidence from Alcator C-Mod[27] and ASDEX Upgrade[28] based on 1D radial impurity transport codes that the impurity density profiles in the pedestal region are well described by standard neoclassical transport processes. This is somewhat unexpected in the pedestal region, since the neoclassical transport coefficients used may not be strictly valid in the pedestal region where $\rho_{\theta,i} \sim L_\perp$.

STRAHL[29], a 1D impurity transport code, was used as a convenient tool to model the impurity density radial profile (ignoring poloidal asymmetries). STRAHL self-consistently solves for the flux-surface averaged impurity density given diffusion and convection coefficients. It solves for multiple charge states, including atomic physics effects of ionization,

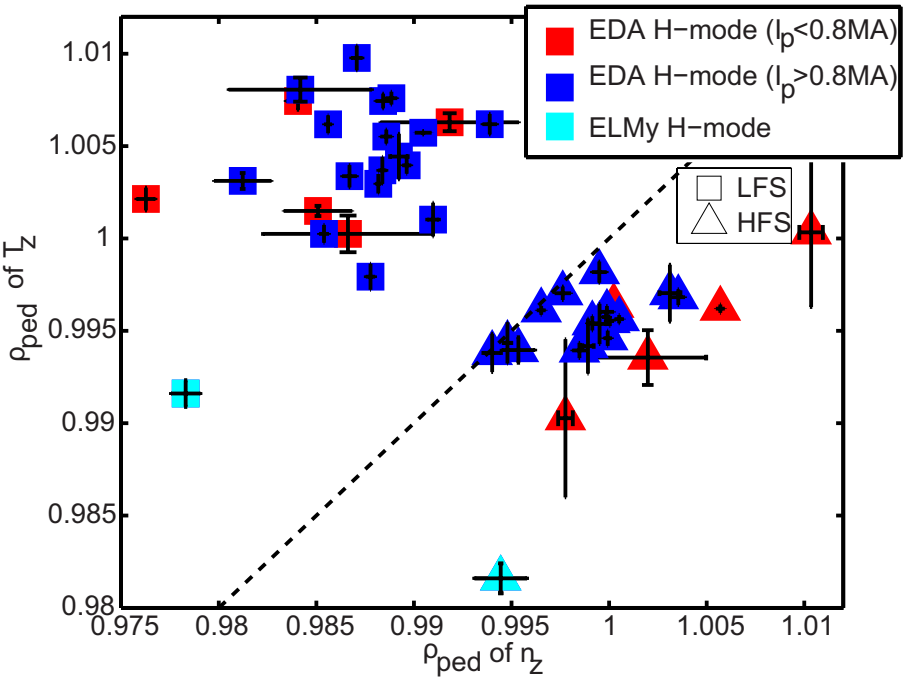

FIG. 9: Pedestal locations (ρ_{ped}) of the impurity temperature and density. The LFS has a density pedestal shifted inward significantly from the measured temperature pedestal

recombination, and charge-exchange. Standard neoclassical diffusion (D_z) and convection (V_z) coefficients[30] are calculated in STRAHL using the NEOART package[29]:

$$\begin{aligned} D_z^{PS} &= \frac{\langle RB_\zeta \rangle^2}{(\partial\psi/\partial r)^2} \left(\langle B^{-2} \rangle - \langle B^2 \rangle^{-1} \right) B^2 \rho_i^2 \nu_{ii} K^{PS} \\ V_z^{PS} &= D_z^{PS} Z \left[\frac{1}{L_{n_i}} + \gamma_T \frac{1}{L_{T_i}} \right]. \end{aligned} \tag{6}$$

where $T_z = T_i$ is assumed so that $\rho_z^2 \nu_{zi} = \rho_i^2 \nu_{ii}$. The gradient scale lengths here can be positive or negative, $L_y = y/(\partial y/\partial r)$. The transport coefficient K^{PS} is near one for trace impurities. The other transport coefficient γ_T is a function of the impurity strength parameter, $\alpha = Z^2 n_z/n_e$, and the collisionality, ν^*. In STRAHL, the radial coordinate actually refers to a normalized flux-volume representation, $r = \sqrt{V/2\pi^2 R_0}$ (here V is the volume between two flux surfaces and R_0 the major radius at the magnetic axis), so that the full shaped magnetic geometry is accounted for (not a cylindrical approximation).The diffusion coefficient is independent of impurity species, but the convective coefficient scales linearly with Z.

As L_{n_i} will always be negative for a monotonically decreasing ion density, main ion

density gradients will cause an *inward* flux of impurities through convection. Temperature gradients, found in the convective term, can either cause an *inward* impurity flux Γ_z if γ_T is positive, or an *outward* impurity flux if γ_T is negative (assuming a monotonic profile for T_i so that L_{T_i} will be negative).

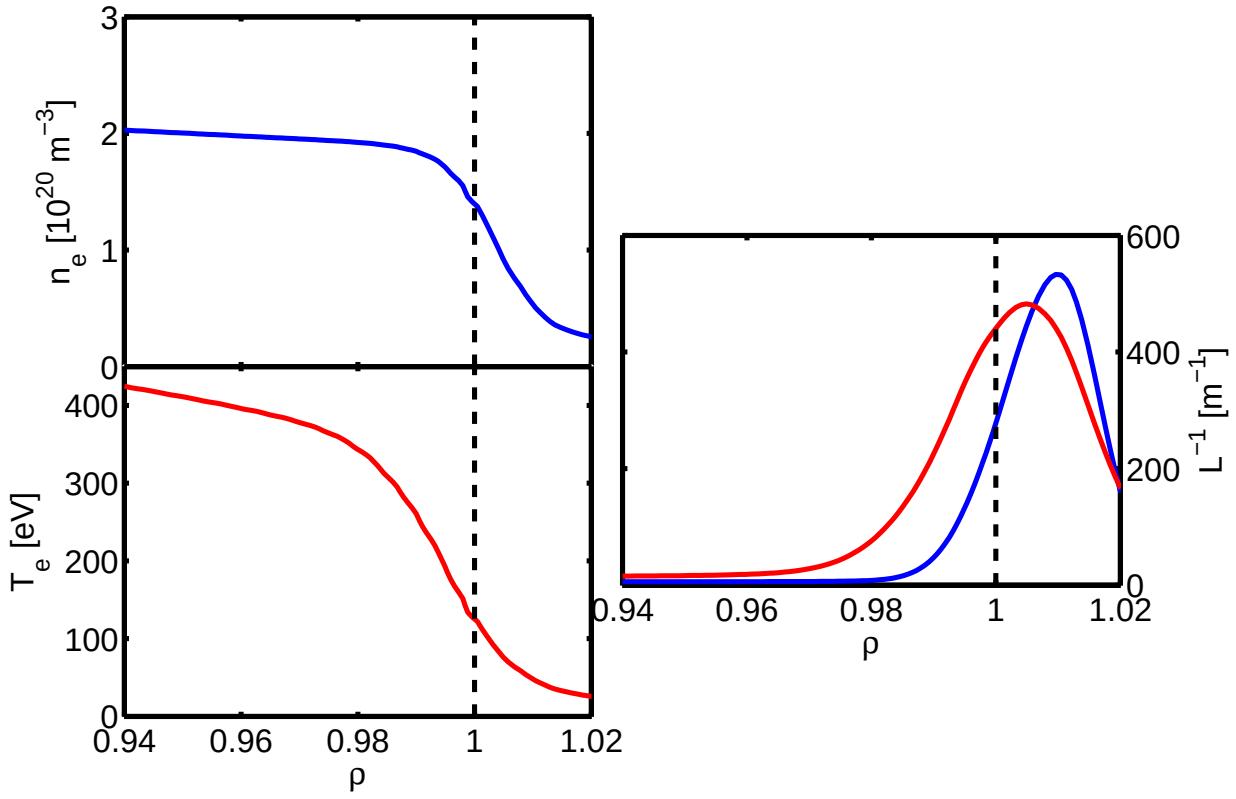

FIG. 10: n_e and T_e inputs into STRAHL, along with a plot of the gradient scale lengths.

Shown in Figure 10 are the measured n_e and T_e profiles from an EDA H-mode which were used as inputs into STRAHL. The D_z and V_z, are shown in Figure 11. Outside the pedestal region $0.972 < \rho < 1.03$ the D_z has been increased to typical levels of anomalous diffusion. The convection V_z was slightly constrained in the region $0.98 \lesssim \rho \lesssim 0.995$ to be less than zero, otherwise peaked impurity profiles resulted.

The resulting STRAHL-simulated B^{5+} density profile is shown in Figure 12, along with impurity densities measured at the LFS and HFS in red and green respectively, and the scaled electron density in orange. The simulated $\langle n_{B^{5+}} \rangle$ appears consistent with the measured HFS $n_{B^{5+}}$. But the LFS measured profile is much further shifted in.

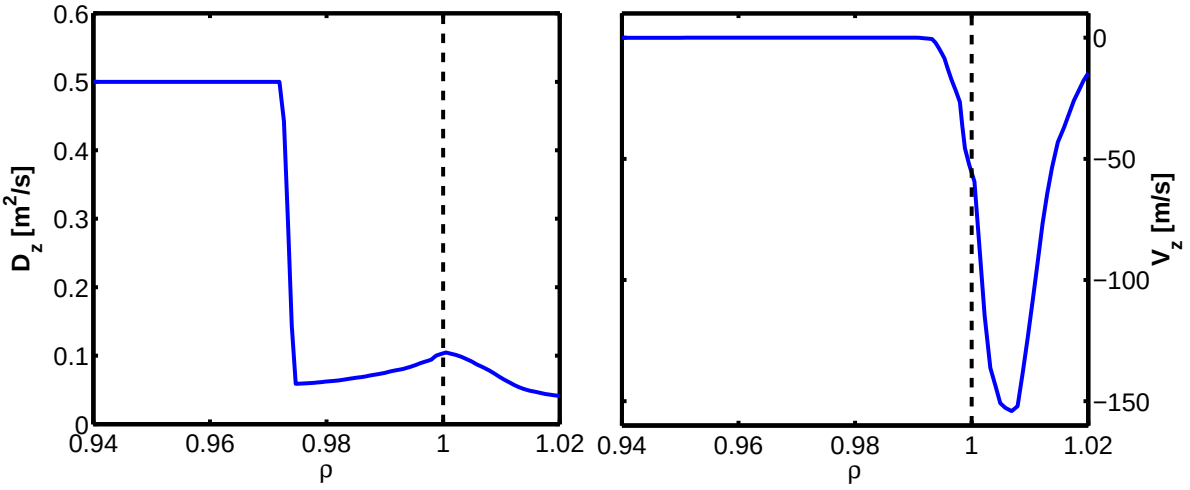

FIG. 11: D_z and V_z^{conv} inputs into STRAHL. Values for $\rho > 0.98$ are neoclassical values, except that V_z^{conv} was forced to be less than zero where V_z^{conv}/D_z was positive, otherwise large impurity peaking was predicted. Outside of the pedestal region, anomalous diffusion values are used.

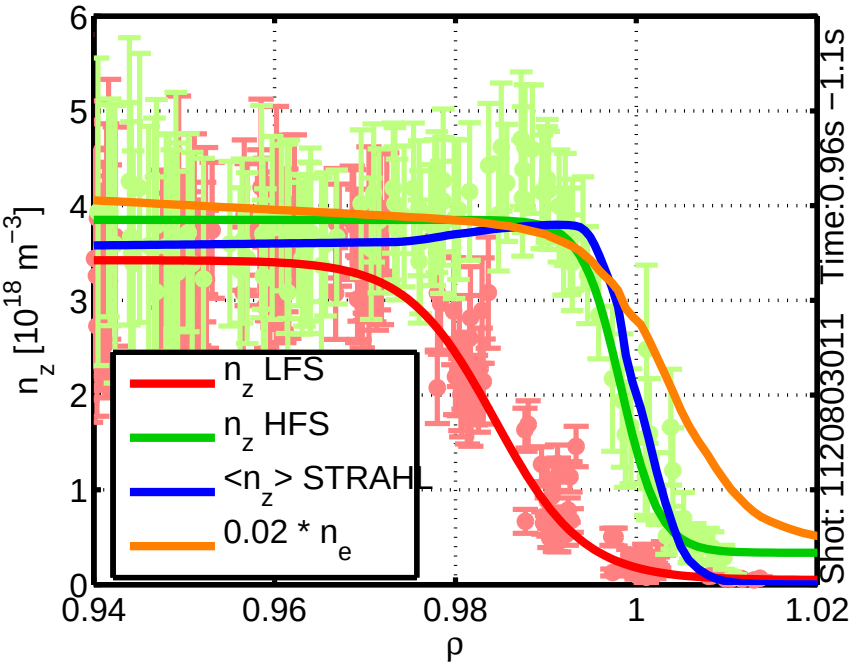

FIG. 12: STRAHL simulated B^{5+} impurity density, along with measured LFS and HFS impurity density, and scaled electron density n_e.

VII. DRIVES FOR IN-OUT IMPURITY ASYMMETRIES

We now explore candidate mechanisms which can cause the observed pedestal B^{5+} impurity density: (1) localized boron particle sources from the inner-wall, (2) fluctuation-driven transport, or (3) increased collisional radial transport.

A. Impurity Sources

One hypothesis is that a localized source of impurities at the HFS is causing a build-up of impurity density there. Such a poloidally asymmetric source could be caused by, for example, sputtering from the inner-wall of the tokamak. The outer-wall has much less material surfaces in close contact with the plasma since non-axisymmetric limiters are used, and the LFS impurity density is measured far from material surfaces, in comparison with the HFS impurity measurements which are typically less than 2 cm away from the inner wall. However, these impurity neutrals would have to ionize up to B^{5+}, and be radially transported faster than the parallel equilibration time.

Already we have some empirical evidence that such a localized source is NOT the cause of the impurity density asymmetry. First, boron is a non-recycling impurity. It is well screened from the core plasma when injected from the inner-wall or divertor[31,32] (i.e. it's mean-free path from these locations is shorter than the gap between the wall and the separatrix). Qualitatively this is thought to be due to the inner-wall acting as a continuous particle sink, though SOL flows may also play an important role. Second, the pedestal impurity density in I-mode and L-mode show no impurity density asymmetry, even though similar levels of ICRF power can be present[1]. Nevertheless, sputtering from the inner-wall in these different plasma operation modes is not well studied, and may well be enhanced in H-mode plasmas. Perhaps, if radial transport is enhanced only in H-mode (e.g. by a particle pinch), the effect of a localized impurity source would only become apparent in H-mode, in the pedestal region at least.

In order to further investigate whether localized impurity sources could cause the in-out impurity density asymmetry, dedicated experiments were devised to change conditions at the inner-wall, decreasing or increasing the source, and monitoring any changes in the measured in-out impurity density asymmetry in the pedestal. On C-Mod, the gap between the

separatrix and the inner-wall is normally ∼10 mm in diverted plasmas. For these experiments, the gap was nominally set to 14 mm, then reduced to 2 mm over a time period of 400 ms, in an effort to increase the particle and heat flux to the inner-wall, thus enhancing the boron erosion from the inner-wall.

For these experiments, the boron source from the inner-wall was monitored by imaging the BII line (412.2 nm), with optical views from the A-side periscope, which are approximately radial views focused on the inner wall, at varying heights[8]. The D_γ line (433.2 nm) was measured in the same spectra, allowing comparison of the relative increase of boron particle flux compared to deuterium particle flux[8]. These spectral lines were measured using an $f/4$ Czerny-Turner spectrometer, with a 600 lines/mm grating.

Example time traces of the BII radiance and inner gap in a discharge where the inner gap was decreased is shown in Figure 13. As the inner-gap decreases, a concurrent increase in the BII line is seen for the views near the inner-wall midplane (Z=0 cm), while views higher on the inner-wall are unchanged. These views where there was an increase in the BII radiance correspond exactly to the regions of the wall which intercepted open field lines connected from the outer-wall midplane SOL.

The boron particle flux, Γ_z, and the measured line-integrated emissivity, I_{BII} (i.e. radiance) are related by the S/XB coefficients[33], $\Gamma_z = 4\pi\,(S/XB)_{BII}\,I_{BII}$. The S/XB coefficient can not be determined exactly for this discharge, as it depends on n_e and T_e, which were not measured at the inner-wall. However, the S/XB coefficient for BII is relatively insensitive[8] to changes in n_e. Assuming at the point of emission that T_e stays constant (since the B^{1+} ionization stage will exist at a relatively fixed T_e), or at the least that T_e only increases as the inner gap is decreased, the S/XB coefficient will only increase. We therefore conclude that the increase in BII emission with decreasing inner gap, Figure 13, does indeed indicate that the boron source is increasing in the SOL at the inner-wall midplane.

Having shown that the boron source is increasing as the inner gap decreases, we now look at the B^{5+} measurements in the pedestal region to determine if there is an observable increase at the HFS, as would be expected if the boron source was rapidly transported radially before symmetrizing on a flux surface. We show in Figure 14 the B^{5+} density profiles over the entire inner gap scan. Figure 15 shows the B^{5+} density value near the top of the HFS pedestal, $\rho \sim 0.972$. As can be seen, $n_{B^{5+}}$ in the pedestal region doesn't increase as the inner gap decreases, despite the increasing boron source. We conclude from these

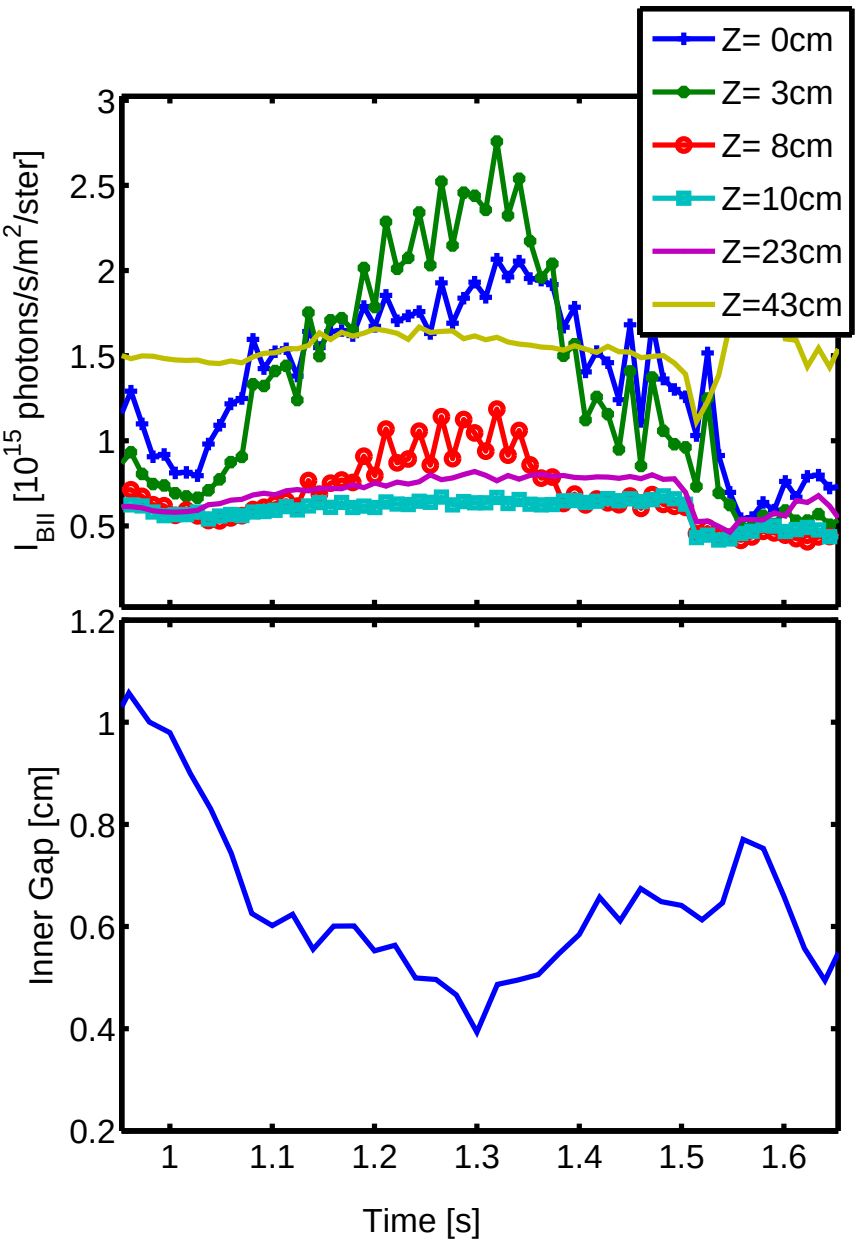

FIG. 13: BII radiance at the inner wall at different heights during inner gap scan.

measurements that even if there is a strong, local boron source coming from the inner-wall, this does not cause a local increase of the fully ionized boron (B^{5+}) in the pedestal region and therefore does not explain the in-out impurity density asymmetry.

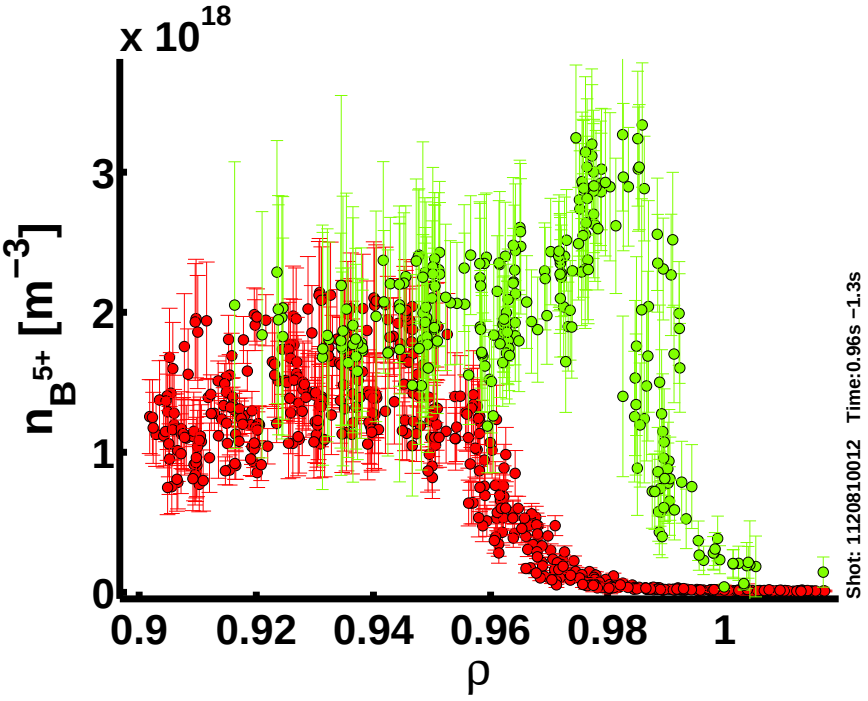

FIG. 14: B^{5+} density during inner gap scan. LFS in red, HFS in green.

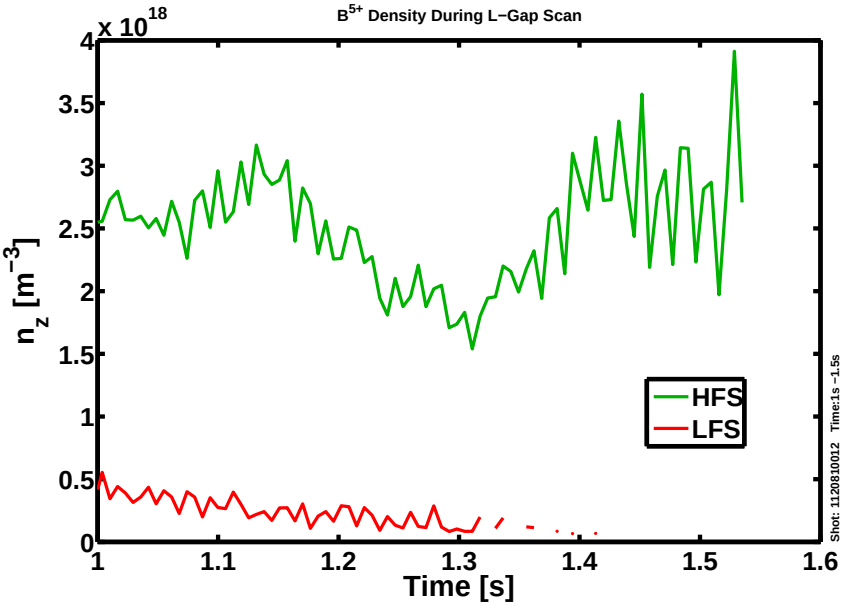

FIG. 15: B^{5+} density near the pedestal top ($\rho \sim 0.972$) during the inner gap scan.

B. Fluctuation Driven Transport

Broadband fluctuations of varying levels are present in the pedestal of the three main types of H-modes in Alcator C-Mod (EDA, ELM-free and ELMy). In addition, the EDA

H-mode[34] exhibits a quasi-coherent mode (QCM) radially located in the pedestal region, but poloidally localized to the LFS. The QCM is correlated with enhanced particle transport in the pedestal. Edge-localized quasi-coherent fluctuations have also recently been observed between ELMs on C-Mod[35], with properties suggestive of kinetic ballooning modes, and which likely provide pedestal-limiting transport in the same manner as the QCM in EDA H-mode. It could be hypothesized then that ballooning modes in the pedestal are responsible for the in-out impurity density asymmetry. The crucial evidence contradicting this hypothesis is that the fluctuations are greatly reduced or suppressed during ELM-free H-modes, but the impurity asymmetry is just as strong.

Figure 16 shows example fluctuating amplitude frequency spectra measured with phase contrast imaging (PCI)[36], for L-mode, I-mode, EDA H-mode, and ELM-free H-mode. The ELM-free H-mode has significantly reduced broadband fluctuations at lower frequencies, although near $f = 120$ kHz rises above L-mode and I-mode to match the EDA H-mode levels. Investigations of fluctuations using Gas Puff Imaging (GPI), which is a measurement local to the LFS midplane, also showed[37] that ELM-free H-mode has a strong overall reduction in fluctuating power in the pedestal region, while the EDA H-mode fluctuation levels are near those of L-mode, with a strong peak due to the quasi-coherent mode (QCM, the peak near 80 kHz in Fig. 16).

This overall reduction in the fluctuations in ELM-free H-mode (widely observed also on other tokamaks) leads one to expect reduced radial transport (although phase relation may also need to be considered). Since the in-out impurity density asymmetry persists in the ELM-free H-mode[8], it seems unlikely that fluctuation-driven transport localized to the LFS is the primary cause for the in-out impurity density asymmetry we observe in the pedestal region.

C. Transport Timescales and Poloidal Transport Asymmetry

In the presence of strong gradients in density and temperature, the collisional radial transport can become comparable to parallel transport. This can cause an impurity density asymmetry if the radial transport is poloidally asymmetric. Impurities can be locally expelled or pulled inwards, similar to the effect of ballooning transport caused by fluctuations.

Here we explore the possibility of poloidally asymmetric, neoclassical radial transport

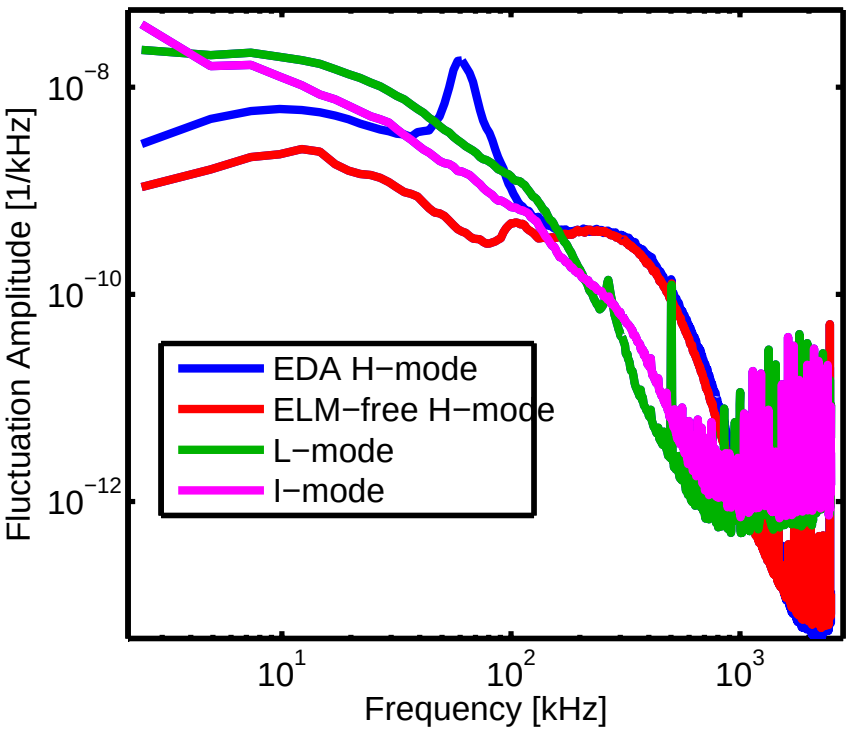

FIG. 16: Electron density fluctuation frequency spectra, measured with PCI. Note the large reduction in fluctuation amplitude in the ELM-free H-mode.

becoming comparable to the parallel transport processes for impurities. We make estimates for the transport time scales, and also discuss the poloidal variation of those timescales. We consider two separate processes that work to symmetrize density on a flux surface: parallel diffusion and poloidal convection. Note that toroidal rotation will not play a role if the density asymmetry is axisymmetric, since then $\nabla \cdot n_z V_{z\zeta} = 0$. We then compare these timescales to the radial transport timescale estimated from standard neoclassical theory. This represents the *minimum* level of radial impurity transport we can expect.

Table I lists the timescales of interest and their respective equations. The parallel transport timescale is taken to be a diffusive process, as impurities are highly collisional in the pedestal region. The parallel diffusion coefficient is taken to be $D_{\parallel,z} = v_{th,z}^2/\nu_{zi}$. Note that only impurity-ion collisions are included, as they are the only collisions that will lead to diffusion (self-collisions will not). The parallel length scale is taken to be half the parallel transit length, $L_\parallel \sim \pi q R_0$, as we are interested in the time to equilibrate between the LFS and HFS. Poloidal timescales are calculated using the measured impurity poloidal velocity, V_θ. The

Timescales	
Parallel	$\tau_{\parallel} \sim \frac{L_{\parallel}^2}{D_{\parallel,z}}$
Poloidal	$\tau_{\theta} \sim \frac{L_{\theta}}{V_{\theta}}$
Radial	$\tau_r \sim \frac{L_r}{\left\lvert -D_z \frac{1}{n_z}\frac{\partial n_z}{\partial r} + V_z^{conv} \right\rvert}$
Ionization	$\tau_{ion} \sim \sum_z \frac{1}{n_e S_{ion}^z}$

TABLE I: Equations used for impurity particle transport timescales

radial transport timescale includes diffusion and also convection, which can be important in the pedestal region. The scale length L_r is the perpendicular gradient scale length, here the impurity density gradient scale length is used, $|L_r| = n_z \left|\frac{dn_z}{dr}\right|^{-1}$. Radial diffusion and convection coefficients are calculated from the standard neoclassical form, Equation 6. The ionization time we calculate here is not the true source transport time but rather the time it takes to completely ionize a boron neutral, i.e. the sum of the individual ionization times of the individual ionization stages[38].

Core Pfirsch-Schlüter calculations for the ions assume the poloidal variation of the density and temperature is weak compared to the poloidal variation of the magnetic field. However, since in the pedestal the poloidal ion gyroradius can become comparable to the scale lengths, stronger poloidal variation occurs. For collisional impurities it is possible then to have $\tau_{//} > \tau_{\theta} > \tau_r$ when $qR_0/\lambda_z > L_{\perp}/\rho_{\theta,z}$, where λ_z is the impurity mean free path.

1. Timescale Example

These timescales of interest are plotted in Figure 17 for a 1 MA EDA H-mode, with the bottom graph showing the LFS and HFS impurity density profiles, from which the gradient scale lengths L_{n_z} were calculated. The radial transport timescale in orange was calculated using a flux-surface averaged impurity density, assuming a dominant in-out asymmetry ($n_z = \langle n_{z,0} \rangle (1 + n_1 \cos\theta)$). As a limit, the LFS and HFS n_z profiles were used separately to calculate τ_r, and are plotted in the thinner orange lines. As the poloidal variation of the diffusion and convection transport coefficients are not well know, the flux averaged quantities were used. The poloidal transport time scale τ_θ was calculated using the measured LFS/HFS poloidal velocities, and assuming in between that $V_{z\theta}$ varies as $V_{z\theta} = K_z(\psi)B_\theta/n_z$. Again, as a limit τ_θ was also calculated with LFS and HFS measured $V_{z\theta}$, and are shown in the thinner purple lines.

Several interesting features are apparent. The radial transport becomes faster than the diffusive parallel transport near the top of the LFS impurity density profile. However, the poloidal transport can still act to symmetrize the impurity density on the flux surface. The radial transport process is comparable to the poloidal timescale in the region beginning at $\rho \approx 0.98$, which is near the T_e pedestal top. This suggests that the impurity particle transport can not be treated as a 1D problem, but rather we must face up to the 2D, perpendicular and parallel coupled transport equation. The radial transport timescale becomes faster than the poloidal at $\rho \approx 0.992$, near the n_e and n_{zH} pedestal tops. In principle, this separation of timescales may again allow a 1D treatment of the radial transport, using local gradients instead of flux-surface averaged. As could be expected, the ionization time τ_{ion} is faster than all other processes in the core most regions. However, for $\rho > 0.992$ both the radial and poloidal transport timescales become faster than the ionization, potentially meaning sources in this region can be transported inward before completely ionizing.

While the radial transport timescale we've shown in Figure 17 is based on a flux-surface averaged diffusion and convection coefficient, in reality the radial transport flux varies strongly with poloidal position[17,29,39]. In regions of low radial transport compared to parallel or poloidal transport, such as the core, this poloidal variation of radial transport doesn't matter, since the parallel transport is so fast that impurities will sample all of the flux surface, averaging out the poloidal variation in radial transport. However, when the radial

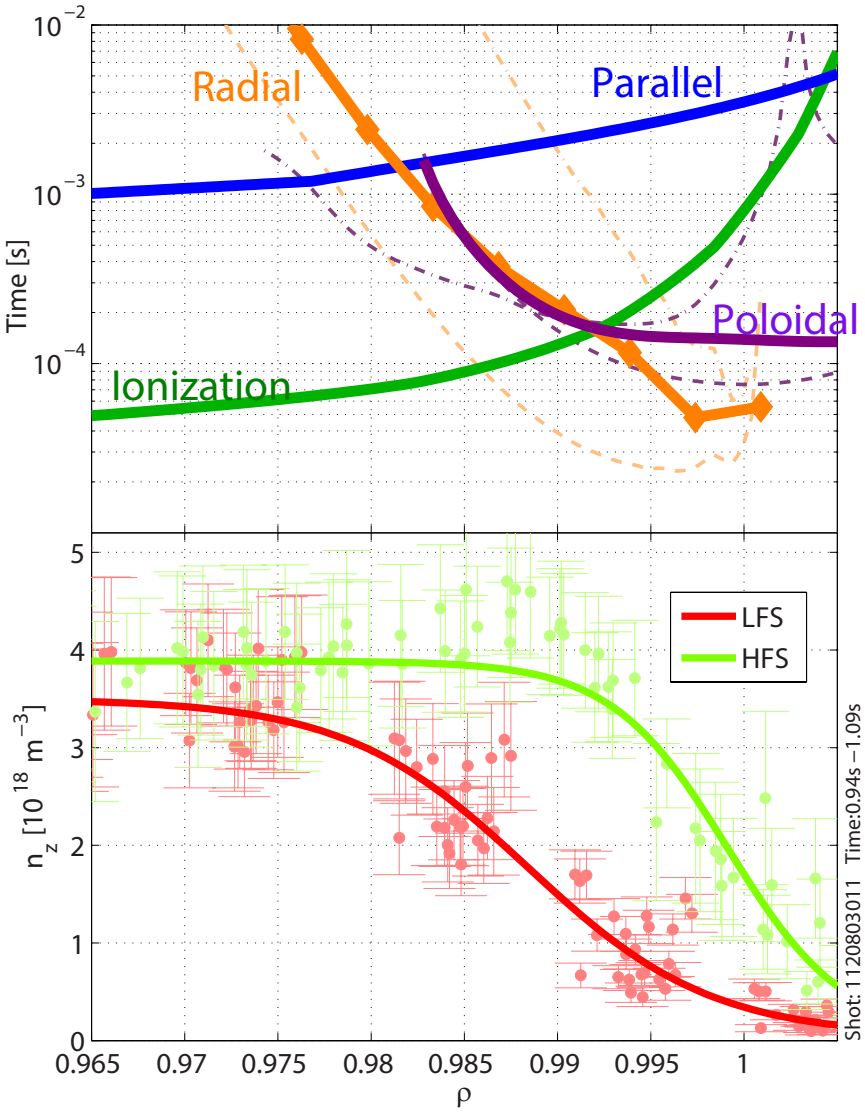

FIG. 17: Timescales for a 1 MA EDA H-mode. LFS/HFS impurity density profiles are also shown.

transport process happens on a timescale faster than that of parallel or poloidal, impurities will start to only sample the radial transport at the poloidal location where they entered the region of strong radial transport, giving rise to impurity density asymmetries. Similar timescale estimates were found for ASDEX-Upgrade H-mode plasmas[28].

The timescales for an I-mode discharge are shown in Figure 18. The picture is qualita-

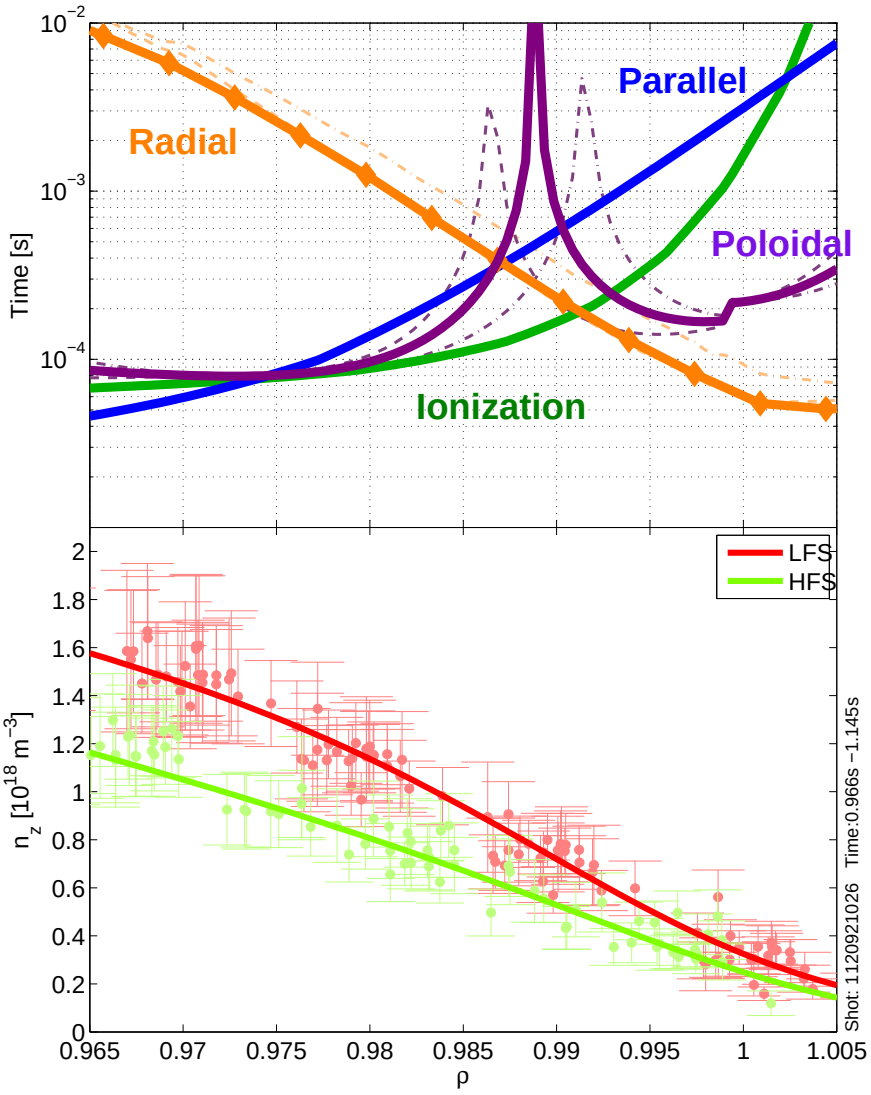

FIG. 18: Timescales for a 1.3 MA I-mode. LFS/HFS impurity density profiles are also shown.

tively similar: the flux-surface average radial transport is close to or faster than the poloidal transport time in the region of the temperature pedestal ($\rho > 0.98$). Yet as also shown in Figure 18, the impurity density is basically symmetric between the LFS and HFS, seemingly unaffected by the increased radial transport. It is therefore clear that the *absolute* level of the radial transport alone can't account for the asymmetry; the *poloidally asymmetric* part of the radial transport must become faster than the poloidal or parallel transport.

A possible driver of significant poloidally asymmetric radial transport in H-mode but not I-mode is the main ion density pedestal. There is a robust collisional transport effect of n_i gradients driving *inward* convection of impurity particle flux (see Equation 6). Because H-modes have a strong main ion density pedestal, and I-modes do not, heuristically we can expect a stronger inward impurity particle flux in H-mode plasmas. This is also a potential mechanism for the empirical observation that the global impurity confinement time is longer in H-mode than in I-mode[40]. Additionally, because of the poloidal variation in n_i, inferred from the T_z asymmetry (see Figure 2), in H-mode a strong inward radial impurity flux driven by n_i gradients will be located further inward on the LFS, since the n_i pedestal is located further inward. Because the poloidal variation of n_i is much less in I-mode than H-mode, this could even further enhance inward impurity particle flux at the LFS in H-mode, and drive stronger in-out impurity density asymmetries.

The above discussion on the role of the main ion gradient driving inward radial impurity flux preferentially at the LFS, with stronger n_i gradients further inward at the LFS due to the poloidal variation of n_i, are suggestive only, and haven't been used yet in a transport code to show that they do reproduce the measured poloidal variation in impurity density. To fully unravel these differences, a more complete impurity modelling retaining 2D effects ($\tau_r \sim \tau_\theta$, and $\rho_{\theta,i} \sim L_{n_i}, L_{T_i}$) is necessary.

VIII. DISCUSSION

There is a commonly held belief in the tokamak community that standard, local neoclassical transport can explain the impurity transport in the pedestal region[27,28,41]. The findings shown here call this belief into question, and warrant further investigations into the subject with experiment, theory, and simulation. In C-Mod, radial transport appears to be more important in the pedestal region than standard neoclassical physics would predict, though it is not clear if the radial transport effects were retained, how different the impurity transport would be in an average sense from the standard picture. Certainly if radial impurity transport is large enough compared to parallel or poloidal transport, and enhanced at specific poloidal locations, this could provide an effective "hole" in the transport barrier through which impurities will preferentially enter or exit.

Comparisons with other tokamaks are needed. In particular, ASDEX Upgrade has a

similar CXRS system as C-Mod[9], allowing similar measurements at the LFS and HFS midplane. In contrast to the Alcator C-Mod findings, on ASDEX Upgrade the impurity density asymmetries are smaller in magnitude[42], and the standard neoclassical transport models well the impurity density[28,42]. Also, the impurity ion temperature pedestal locations align with the radial electric field wells[43], indicating that the ion temperature, ion density, and electrostatic potential are much closer to flux functions than found in the C-Mod pedestal region. While similar collisionalities can be observed in ASDEX Upgrade and C-Mod pedestals, differences between the two devices such as the size of the poloidal Larmor radius compared to the temperature and density scale lengths need to be investigated to determine the cause of the observed differences in poloidal variation of pedestal quantities.

Already important simulation and theoretical work are forthcoming, focused on including the non-local transport effects caused by large gradients in the density and temperature[17,23,44–46]. Analytical formulas for pedestal transport are beneficial, but ultimately the complexity of the problem will likely necessitate a computational solution. The initial results presented here from the XGCa code show promise in correctly capturing the poloidal variation of the main ion temperature and electric potential in the pedestal region of Alcator C-Mod. Preliminary XGCa results of ASDEX-Upgrade suggest the ion temperature has a much smaller poloidal asymmetry than on Alcator C-Mod. Further work with such codes will allow comparisons of simulated impurity transport to experimental observation, and ultimately help identify the driving physics.

IX. SUMMARY

We have explored the poloidal asymmetries which arise in impurity density and temperature in the H-mode pedestal region. Due to the fact that the observed impurity ion temperature and electric potential could not simultaneously be flux functions[7], an updated technique to align the LFS and HFS profiles was implemented, which assumed that the total pressure is constant on a flux surface, and that the electrons are adiabatic. With this alignment, the measured HFS and LFS E_r wells closely align, retaining a small asymmetry, and the LFS impurity ion temperature exceeds the HFS values by up to 70%. In-out impurity density asymmetries in H-mode plasmas have a peak asymmetry value of 2.5 to 9, always with higher densities at the HFS. The n_z pedestal on the LFS shows marked changes with

changing plasma current, namely that the width increases, and the location shifts in slightly with decreasing plasma current. A comparison of pedestal locations of n_z and T_z at the LFS shows that the n_z pedestal is consistently further shifted in than the T_z pedestal, whereas for the HFS the pedestal location of the two quantities generally align.

An in-out asymmetry of electron density in the H-mode pedestal region is inferred from the measured electric potential asymmetry, with higher electron densities at the HFS. Measurements of the D_α emission at the LFS and HFS are at least consistent with such a poloidal variation in n_e.

First simulations of a C-Mod H-mode plasma with the gyrokinetic neoclassical code XGCa show good agreement with experiment in the magnitude and direction of poloidal variation in main ion density, main ion temperature, and electric potential.

One-dimensional impurity modelling with STRAHL shows that, using standard neoclassical physics, the predicted flux-surface averaged impurity density is similar to the experimental HFS profile, but its strong discrepancies with the LFS profile would require other anomalous radial transport mechanisms are present at the LFS.

Investigating the origin of the impurity density asymmetry, it was shown that localized sources from the inner-wall, and from the LFS SOL do not affect the level of B^{5+} in the pedestal region arguing against locals sources as the cause of the asymmetry. Fluctuations were similarly discounted as the chief cause of the n_z asymmetry, because ELM-free H-modes exhibit much reduced electron density fluctuation levels, but still develop an impurity density asymmetry.

Radial transport processes estimated using standard neoclassical transport coefficients were shown to give comparable timescales to measured poloidal transport, and much faster than parallel transport timescales, signifying again that a 2D treatment of impurity particle transport may be necessary. However, I-mode plasmas exhibited similar coupling of timescales, but without in-out n_z asymmetries, indicating that the radial transport magnitude is not alone the determining factor in the impurity density asymmetry. It was highlighted that neoclassical theory predicts that main ion density gradients drive an *inward* convection of impurities, which, when considered along with the poloidally varying n_i in H-mode, could drive a stronger inward impurity particle flux at flux surfaces further inward at the LFS, leading to impurity density asymmetries. The presence of an inward impurity flux driven by the main ion density pedestal is also consistent with the observed global im-

purity confinement being long in H-mode, while being short in I-mode. While this appears to be the most plausible mechanism for driving the impurity density asymmetry, actual impurity transport modelling with coupled 2D radial and poloidal/parallel impurity transport is needed to determine if such a mechanism can reproduce the measured impurity profiles.

X. ACKNOWLEDGMENTS

This work was supported by US DOE Coop. Agreement No. DE-FC02-99ER54512. C. Theiler was also supported by the Swiss National Science Foundation (SNSF). XGCa simulations were made possible by SciDAC grants jointly between the US DOE Office of Fusion Energy Science and the Office of Advanced Scientific Computing Research under DE- FG02-06ER54845, by a grant from the US DOE Office of Fusion Energy Science under DE-FG02-86ER53223, and by a contract under DE-AC02-09CH11466.

XI. REFERENCES

REFERENCES

[1]R. M. Churchill, B. Lipschultz, and C. Theiler, Nuclear Fusion, **53**, 122002 (2013), ISSN 0029-5515.

[2]P. Helander, Physics of Plasmas, **5**, 3999 (1998).

[3]T. Fülöp and P. Helander, Physics of Plasmas, **8**, 3305 (2001).

[4]M. Landreman, T. Fülöp, and D. Guszejnov, Physics of Plasmas, **18**, 092507 (2011).

[5]K. H. Burrell and S. K. Wong, Nuclear Fusion, **19**, 1571 (1977), ISSN 0029-5515.

[6]D. G. Whyte, A. E. Hubbard, J. W. Hughes, B. Lipschultz, J. E. Rice, E. S. Marmar, M. Greenwald, I. Cziegler, A. Dominguez, T. Golfinopoulos, N. Howard, L. Lin, R. M. McDermott, M. Porkolab, M. L. Reinke, J. Terry, N. Tsujii, S. Wolfe, S. Wukitch, Y. Lin, and t. A. C.-M. Team, Nuclear Fusion, **50**, 105005 (2010), ISSN 0029-5515.

[7]C. Theiler, R. M. Churchill, B. Lipschultz, M. Landreman, D. R. Ernst, J. W. Hughes, P. J. Catto, F. I. Parra, I. H. Hutchinson, M. L. Reinke, A. E. Hubbard, E. S. Marmar, J. T. Terry, and J. R. Walk, Nuclear Fusion, **54**, 083017 (2014), ISSN 0029-5515.

[8]R. M. Churchill, *Impurity Asymmetries in the Pedestal Region of the Alcator C-Mod Tokamak*, Ph.d. thesis, Massachusetts Institute of Technology (2014).

[9]R. M. Churchill, C. Theiler, B. Lipschultz, R. Dux, T. Putterich, and E. Viezzer, Review of Scientific Instruments, **84**, 093505 (2013), ISSN 00346748.

[10]J. W. Hughes, D. A. Mossessian, A. E. Hubbard, E. S. Marmar, D. Johnson, and D. Simon, Review of Scientific Instruments, **72**, 1107 (2001).

[11]R. M. McDermott, B. Lipschultz, J. W. Hughes, P. J. Catto, A. E. Hubbard, I. H. Hutchinson, R. S. Granetz, M. Greenwald, B. LaBombard, K. Marr, M. L. Reinke, J. E. Rice, D. Whyte, and the Alcator C-Mod Team, Physics of Plasmas, **16**, 056103 (2009), ISSN 1070664X.

[12]K. D. Marr, B. Lipschultz, P. J. Catto, R. M. McDermott, M. L. Reinke, and A. N. Simakov, Plasma Physics and Controlled Fusion, **52**, 055010 (2010), ISSN 0741-3335.

[13]J. Neuhauser, D. Coster, H. U. Fahrbach, J. C. Fuchs, G. Haas, A. Herrmann, L. Horton, M. Jakobi, A. Kallenbach, M. Laux, J. W. Kim, B. Kurzan, H. W. Müller, H. Murmann, R. Neu, V. Rohde, W. Sandmann, W. Suttrop, E. Wolfrum, and t. A. U. Team, Plasma Physics and Controlled Fusion, **44**, 855 (2002), ISSN 0741-3335.

[14]B. LaBombard, "Te at the Separatrix in C-Mod," Tech. Rep. (MIT PSFC, 2003).

[15]F. L. Hinton and R. D. Hazeltine, Reviews of Modern Physics, **48**, 239 (1976).

[16]P. Helander and D. J. Sigmar, *Collisional Transport in Magnetized ...* (Cambridge University Press, 2005).

[17]J. D. Callen, R. J. Groebner, T. H. Osborne, J. M. Canik, L. W. Owen., A. Y. Pankin, T. Rafiq, T. D. Rognlien, and W. M. Stacey, Nuclear Fusion, **50**, 064004 (2010), ISSN 0029-5515.

[18]A. N. Simakov and P. J. Catto, Physics of Plasmas, **10**, 4744 (2003), ISSN 1070664X.

[19]S. P. Hirshman and D. J. Sigmar, Nuclear Fusion, **21** (1981), ISSN 0029-5515, doi: 10.1088/0029-5515/21/9/003.

[20]Note the potential asymmetry in the T_z-alignment would indicate a larger total pressure at the LFS, which the ion inertia from toroidal rotation could balance (Equation 3). However, a sonic ion toroidal flow would be required. Measurements of impurity ion toroidal flow indicate subsonic toroidal flow.

[21]C. S. Chang, S. Ku, P. H. Diamond, Z. Lin, S. Parker, T. S. Hahm, and N. Samatova, Physics of Plasmas, **16**, 056108 (2009), ISSN 1070664X.

[22]E. A. Belli and J. Candy, Plasma Physics and Controlled Fusion, **50** (2008), ISSN 0741-3335, doi:10.1088/0741-3335/50/9/095010.

[23]M. Landreman and D. R. Ernst, Plasma Physics and Controlled Fusion, **54**, 115006 (2012).

[24]T. S. Pedersen, R. S. Granetz, E. S. Marmar, D. Mossessian, J. W. Hughes, I. H. Hutchinson, J. Terry, and J. E. Rice, Physics of Plasmas, **9**, 4188 (2002).

[25]The results plotted here are taken directly from Ref[24], and represent the mean values across several hundreds of discharges. The Pedersen paper quotes the pedestal location difference in real space, ΔR_{mid}. These were adjusted for the 3mm calibration offset mentioned in the paper, then converted to $\Delta\rho$.

[26]J. W. Hughes, B. LaBombard, D. A. Mossessian, A. E. Hubbard, J. Terry, T. Biewer, and t. A. C. M. Team, Physics of Plasmas, **13** (2006), doi:10.1063/1.2180748.

[27]T. S. Pedersen, R. S. Granetz, A. E. Hubbard, I. H. Hutchinson, E. S. Marmar, J. E. Rice, and J. Terry, Nuclear Fusion, **40**, 1795 (2000), ISSN 0029-5515.

[28]T. Pütterich, R. Dux, M. A. Janzer, and R. M. McDermott, Journal of Nuclear Materials, **415**, S334 (2011), ISSN 00223115.

[29]R. Dux, "STRAHL User Manual," (2006).

[30]The form for V_z used here is that for mixed collisionality (i.e. low collisionality main ions, and Pfirsch-Schlüter impurities), appropriate for the C-Mod pedestal, and differs from the Rutherford form[47] used in previous C-Mod studies[27], which is for impurities in regions with highly collisional main ions.

[31]G. M. McCracken, R. S. Granetz, B. Lipschultz, B. Labombard, F. Bombarda, J. A. Goetz, S. Lisgo, D. Jablonski, H. Ohkawa, J. E. Rice, P. C. Stangeby, J. L. Terry, and Y. Wang, Journal of Nuclear Materials, **241-243**, 777 (1997), ISSN 00223115.

[32]B. Lipschultz, D. A. Pappas, B. LaBombard, J. E. Rice, D. Smith, and S. J. Wukitch, Nuclear Fusion, **41**, 585 (2001), ISSN 0029-5515.

[33]K. H. Behringer, Journal of Nuclear Materials, **145-147**, 145 (1987), ISSN 00223115.

[34]M. Greenwald, N. Basse, P. Bonoli, R. Bravenec, E. Edlund, D. Ernst, C. Fiore, R. Granetz, A. Hubbard, J. Hughes, I. Hutchinson, J. Irby, B. LaBombard, L. Lin, Y. Lin, B. Lipschultz, E. Marmar, D. Mikkelsen, D. Mossessian, P. Phillips, M. Porkolab, J. Rice, W. Rowan, S. Scott, J. Snipes, J. Terry, S. Wolfe, S. Wukitch, and K. Zhurovich, Fusion Science and Technology, **51**, 266 (2007).

[35]A. Diallo, J. Hughes, M. Greenwald, B. LaBombard, E. Davis, S.-G. Baek, C. Theiler, P. Snyder, J. Canik, J. Walk, T. Golfinopoulos, J. Terry, M. Churchill, A. Hubbard, M. Porkolab, L. Delgado-Aparicio, M. Reinke, and A. White, Physical Review Letters,

112, 115001 (2014), ISSN 0031-9007.

[36]L. Lin, M. Porkolab, E. M. Edlund, J. C. Rost, C. L. Fiore, M. Greenwald, Y. Lin, D. R. Mikkelsen, N. Tsujii, and S. J. Wukitch, Physics of Plasmas, **16**, 012502 (2009), ISSN 1070664X.

[37]I. Cziegler, J. L. Terry, J. W. Hughes, and B. LaBombard, Physics of Plasmas, **17** (2010), doi:10.1063/1.3421577.

[38]The ionization rate coefficients for boron were taken from an ADAS data file used in STRAHL (scd00_b.dat), and checked against analytic expressions[48].

[39]V. Naulin, Physical Review E, **71**, 015402 (2005).

[40]N. T. Howard, M. Greenwald, and J. E. Rice, The Review of scientific instruments, **82**, 033512 (2011), ISSN 1089-7623.

[41]R. Dux, A. Loarte, E. Fable, and A. Kukushkin, Plasma Physics and Controlled Fusion, **56**, 124003 (2014), ISSN 0741-3335.

[42]E. Viezzer, T. Pütterich, E. Fable, A. Bergmann, R. Dux, R. M. McDermott, R. M. Churchill, and M. G. Dunne, Plasma Physics and Controlled Fusion, **55**, 124037 (2013), ISSN 0741-3335.

[43]E. Viezzer, in *25th IAEA Conference Proceedings* (2014).

[44]C. S. Chang, S. Ku, and H. Weitzner, Physics of Plasmas, **11**, 2649 (2004).

[45]G. Kagan and P. J. Catto, Plasma Physics and Controlled Fusion, **52** (2010), ISSN 0741-3335, doi:10.1088/0741-3335/52/5/055004.

[46]P. J. Catto, F. I. Parra, and G. Kagan, Plasma Physics and Controlled Fusion, **55**, 045009 (2013).

[47]P. H. Rutherford, Physics of Fluids, **17**, 1782 (1974), ISSN 00319171.

[48]K. L. Bell, H. B. Gilbody, J. G. Hughes, A. E. Kingston, and F. J. Smith, Journal of Physical and Chemical Reference Data, **12**, 891 (1983), ISSN 00472689.